Published in final edited form as:
J Nanomech Micromech. 2013 ; 3(4): . doi:10.1061/(ASCE)NM.2153-5477.0000069.

Poromechanics Parameters of Fluid-Saturated Chemically Active Fibrous Media Derived from a Micromechanical Approach

Anil Misra, M.ASCE[1] **[Professor]**, **Ranganathan Parthasarathy**[2] **[Ph.D. Student]**, **Viraj Singh**[3] **[Ph.D. Student]**, and **Paulette Spencer**[4] **[Professor]**

Anil Misra: amisra@ku.edu

[1]Civil, Environmental and Architectural Engineering Dept. and Associate Director, Bioengineering Research Center (BERC), Univ. of Kansas, 1530 W. 15th St., Lawrence, KS 66045

[2]Bioengineering Graduate Program, Univ. of Kansas, Lawrence, KS 66045

[3]Mechanical Engineering Dept., Univ. of Kansas, Lawrence, KS 66045

[4]Mechanical Engineering Dept. and Director, Bioengineering Research Center (BERC), Univ. of Kansas, Lawrence, KS 66045

Abstract

The authors have derived macroscale poromechanics parameters for chemically active saturated fibrous media by combining microstructure-based homogenization with Hill's volume averaging. The stress-strain relationship of the dry fibrous media is first obtained by considering the fiber behavior. The constitutive relationships applicable to saturated media are then derived in the poromechanics framework using Hill's Lemmas. The advantage of this approach is that the resultant continuum model assumes a form suited to study porous materials, while retaining the effect of discrete fiber deformation. As a result, the model is able to predict the influence of microscale phenomena such as fiber buckling on the overall behavior, and in particular, on the poromechanics constants. The significance of the approach is demonstrated using the effect of drainage and fiber nonlinearity on monotonic compressive stress-strain behavior. The model predictions conform to the experimental observations for articular cartilage. The method can potentially be extended to other porous materials such as bone, clays, foams, and concrete.

Author keywords

Poromechanics; Micromechanics; Osmotic pressure; Swelling; Stress-strain behavior; Drained; Undrained

Introduction

The theoretical analysis of the mechanical behavior of saturated chemically active fiber networks such as soft tissue and hydrogels is an active area of research. Most of the existing models for these materials are generally based on the continuum mixture theory (Truesdell

Correspondence to: Anil Misra, amisra@ku.edu.

and Toupin 1960). The application of the continuum mixture theory to saturated, chemically active media such as biological tissue and hydrogel polymers has been made by numerous authors, notable among them being the biphasic and triphasic theories (Lai et al. 1991; Mow et al. 1980; Wang and Hong 2012; Yoon et al. 2010). These methods have employed continuum mixture theory to determine the constitutive behavior from the Helmholtz free energy. More recently, the influence of fiber orientation and local compression-tension nonlinearity has been implemented into constitutive models (Ateshian et al. 2009; Loret and Simoes 2010).

Saturated fibrous network can be described as porous solid and modeled using principles of poromechanics pioneered by Biot (1941, 1972), who developed the stress-strain relationships for infinitesimal and finite deformations of soil under three-dimensional consolidation. The constitutive relationships in poromechanical theory involve additional material constants apart from the stiffness tensor of the solid matrix phase. These poromechanical parameters, denoted in this paper by B_{ij} and Γ, are necessary to account for the additional degrees of freedom, viz the fluid pressure and the change of fluid content. For linear isotropic materials, parameters B_{ij} and Γ correspond to the constants α and $1/Q$ introduced by Biot (1941). In the models based on the continuum mixture theory, B_{ij} has generally been assigned a value of identity corresponding to Terzaghi's (1925) stress, and the influence of the compressibility of the solid network on Γ is not accounted for explicitly.

In contrast to poromechanics models for chemically inert materials, development of constitutive models for chemically active networks involves additional considerations because of a pore-pressure dependence on chemical potential. Along these lines, models of swelling porous media, such as chemically active clays, that incorporate microscopic considerations of chemical activity and fluid transport have been developed following homogenization methods and continuum mixture theory [see, for example, Bennethum and Cushman (1996), Bennethum et al. (1997), and Moyne and Murad (2003, 2002)]. In addition, there is need to account for (1) nonuniform strain distribution between the solid matrix and pore space; and (2) the effect of nonlinearity of the solid matrix and the influence of evolution in fiber network properties with loading on B_{ij} and Γ. These aforementioned aspects have not been universally accounted for in the existing literature relevant to chemically active fibrous media. In contrast, micromechanics-based approaches have been developed to obtain the poromechanical parameters (de Buhan et al. 1998; Dormieux et al. 2002; Lydzba and Shao 2000) and recently applied to the swelling of bentonite clay (Cariou et al. 2009). These approaches account for nonuniform strain distribution through strain concentrations tensors and the compliance of the solid matrix. For example, strain concentration tensors were determined using self-consistent homogenization, and the resulting model was applied to study the poroelastic behavior of dentin and clays (Dormieux et al. 2003; Misra et al. 2012).

The present work extends the micromechanics-based poromechanics models to fibrous networks by (1) incorporating the discrete nature of the individual fibers through micromechanics-based homogenization; and (2) relating the fiber network description with a poromechanics description. The derived model is applied to investigate the free swelling and the drained and the un-drained behavior of fibrous media, in which the swelling is induced

by chemical activity. A macroscopic chemical potential approach is used to model the effect of chemical activity. The continuum law derived incorporates the effects of fiber elongation properties, buckling, and chemical activity on the coupling constants and the overall material behavior. Consequently, the authors show that while B_{ij} and Γ may be approximated as unity and zero, respectively, at large strains, it is necessary to obtain more accurate estimates, especially when the applied strain is below fiber prestrain.

In the subsequent discussion, the authors first derive the stress-strain relationship for a fiber network using kinematically driven micromechanical methodology (Chang and Misra 1990; Misra and Chang 1993). The homogenized network is then superposed with the fluid phase to derive the overall constitutive relationship, including expressions for the poromechanical parameters B_{ij} and Γ. Finally, the variation in B_{ij} and Γ is investigated for cases of drained and undrained loading with varying fiber nonlinearity for chemically active fiber networks. The intent of the developed model is to describe the observed macroscale mechanical behavior such as (1) postyield stiffening and reduction in Poisson's ratio under drained conditions or slow loading rate (Chahine et al. 2004); and (2) relatively stiff behavior without any yielding and constant Poisson's ratio under undrained conditions and fast loading rates (Oloyede et al. 1992). The developed model shows that these macroscale phenomena are related to the microscale mechanisms such as osmotic swelling because of chemical activity, swelling induced fiber prestrain, fiber-bucking under compression because of the high fiber aspect ratio, and nonuniform strain distribution between the solid and fluid phases. It was found that the developed model predictions show similarity to the experimentally observed data for drained and undrained cases of loading.

Micromechanical Model

A porous material is considered whose solid matrix is a fibrous network as shown schematically in Fig. 1, which depicts the microscopic and continuum scales of dry and saturated fibrous porous media. In general, saturated chemically active porous media have a nonlinear behavior accompanied by large strains. Therefore, an incremental form of Biot's constitutive equations is sought for this media. In this paper, only the nonlinearities that originate from fiber buckling, elongation dependent fiber stiffness, and charge density dependent chemical potential are treated. Nonlinearities from dissipative processes that lead to plastic deformations will be treated in future work. In this case, linearity can be assumed for small increments in stress and strain; thus, superposition is used to derive the incremental constitutive behavior. To proceed, the general loading increment is considered to be a superposition of two cases. In case 1, an increment of Green-Lagrange strain is applied while the increment of interstitial fluid pressure is held at zero, denoted as ($\dot{\varepsilon} \neq 0$, $\dot{p} = 0$). In case 2, the increment of Green-Lagrange strain is held to be zero while an increment of interstitial fluid pressure is applied, denoted as ($\dot{\varepsilon} = 0$, $\dot{p} \neq 0$). Similar superposition has been used for modeling porous media previously (Dormieux et al. 2003, 2002; Misra et al. 2012).

Case 1: ($\dot{\varepsilon} \neq 0$, $\dot{p} = 0$)

Fiber Network Stress—First the macroscopic Cauchy stress, σ_{ij}, of a representative volume element (RVE) of the dry fiber network is written as the volume average of microscopic stresses

$$\sigma_{ij}=\frac{1}{V}\int_V \sigma_{ij}^f dV \quad (1)$$

where V = RVE; and σ_{ij}^f = stress in infinitesimal volume dV. Using Signorini's (1932) theorem and applying Gauss' divergence rule, Eq. (1) can be written as [see Chang and Misra (1989)]

$$\sigma_{ij}=\frac{1}{V}\int_V \sigma_{ik}^f \frac{\partial x_j}{\partial x_k} dV=\frac{1}{V}\int_{\partial V} \sigma_{ik}^f n_k x_j dA - \frac{1}{V}\int_V \frac{\partial \sigma_{ik}^f}{\partial x_k} x_j dV \quad (2)$$

In the absence of body forces and inertial effects, $(\partial \sigma_{ik}^f / \partial x_k)=0$

$$\sigma_{ij}=\frac{1}{V}\int_{\partial V} \sigma_{ik}^f n_k x_j dA=\frac{1}{V}\int_{\partial V} t_i^f x_j dA \quad (3)$$

where the traction vector $t_i^f=\sigma_{ik}^f n_k$; the position vector $x_i = R_i + r_i$, the centroid of the RVE is denoted by R_i; x_i = position vector of one end of the intercepted collagen fiber; and r_i = radius vector of the spherical RVE as shown in Fig. 2. Eq. (3) can now be simplified as

$$\sigma_{ij}=\frac{1}{V}\int_{\partial V} t_i^f (R_j+r_j) dA=\frac{1}{V}\int_{\partial V} t_i^f r_j dA=\frac{1}{V}\int_{\partial V} r_j df_i^f \quad (4)$$

because $\int_{\partial V} t_i^f R_j dA=0$ for centro-symmetrical RVE. Further, the force acting on the infinitesimal area dA, defined as $df_i^f=t_i^f dA$, is given by

$$df_i^f=[A^f \sigma^f(\theta,\phi) n_i] N \xi(\theta,\phi) \sin\theta d\theta d\phi \quad (5)$$

as the product of (1) the force in the fiber, $A^f \sigma^f n_i$, where A^f = fiber area; σ^f = fiber stress; and n_i = unit normal vector expressed in spherical coordinates as the triad $\langle \cos\theta, \sin\theta\cos\phi, \sin\theta\sin\phi \rangle$; and (2) the number of fibers intersecting the infinitesimal area, $dA = \sin\theta d\theta d\phi$, given by $N\xi(\theta, \phi) \sin\theta d\theta d\phi$, where $\xi(\theta, \phi)$ = probability density of the fiber distribution along (θ, ϕ); and N = total number of fibers. Because the average length of a fiber is given as r, the total volume of fibers in the RVE is $NA^f r$. Expressing fiber volume in terms of the fiber volume fraction, γ_f, gets

$$NA^f r=\gamma_f V \quad (6)$$

Combining Eqs. (4), (5), and (6) obtains the following relationship for the RVE Cauchy stress

$$\sigma_{ij}=\gamma_f\int_{\partial V}\sigma^f(\theta,\phi)n_in_j\xi(\theta,\phi)\sin\theta d\theta d\phi \quad (7)$$

The relationship for the increment of the RVE Cauchy stress, $\dot{\sigma_{ij}}$, is now obtained as follows from Eq. (4):

$$\dot{\sigma}_{ij}=-\frac{\dot{V}}{V^2}\int_{\partial V}df_i^f r_j+\frac{1}{V}\int_{\partial V}d\dot{f}_i^f r_j+\frac{1}{V}\int_{\partial V}df_i^f\dot{r}_j \quad (8)$$

where the terms with an over dot (\skew2\dot) denote incremental quantities throughout the paper. From the definition of the Second Piola Kirchhoff stress, $df_i^f=F_{ik}df_k^{f0}$, where the force df_i^f expressed with respect to the current configuration is related to the force df_i^{f0} expressed with respect to the undeformed configuration through the deformation gradient, F_{ik}. Thus

$$d\dot{f}_i^f=\dot{F}_{ik}df_k^{f0}+F_{ik}d\dot{f}_k^{f0} \quad (9)$$

Further, from the definition of the deformation gradient $r_j=F_{jm}r_m^0$

$$\dot{r}_j=\dot{F}_{jm}r_m^0 \quad (10)$$

where r_m^0= position vector in the undeformed configuration. Eq. (8) can now be written as follows:

$$\dot{\sigma}_{ij}=-\frac{\dot{J}}{J^2V_0}F_{ik}\left(\int_{\partial V}df_k^{f0}r_m^0\right)F_{jm}+\frac{1}{V}\int_{\partial V}d\hat{f}_i^f r_j+\frac{1}{JV_0}\dot{F}_{ik}\left(\int_{\partial V}df_k^{f0}r_m^0\right)F_{jm}+\frac{1}{JV_0}F_{ik}\left(\int_{\partial V}df_k^{f0}r_m^0\right)\dot{F}_{jm} \quad (11)$$

where V_0 = undeformed volume of the RVE; J = Jacobian of the deformation gradient such that $V = JV_0$ and $d\hat{f}_i^f=F_{ik}d\dot{f}_k^{f0}$. The Cauchy stress defined in Eq. (4) can be expressed in terms of the Second Piola Kirchhoff stress as follows:

$$\sigma_{ij}=\frac{1}{J}F_{ik}S_{km}F_{jm}=\frac{1}{J}F_{ik}\left(\frac{1}{V_0}\int_{\partial V}df_k^{f0}r_m^0\right)\dot{F}_{jm} \quad (12)$$

Thus, Eq. (11) can be written as

$$\dot{\sigma}_{ij}=-\dot{J}J^{-2}F_{ik}S_{km}F_{jm}+\hat{\sigma}_{ij}+J^{-1}\dot{F}_{ik}F_{ik}S_{km}F_{jm}+J^{-1}F_{ik}S_{km}\dot{F}_{jm} \quad (13)$$

Using the spatial velocity gradient defined as $L_{jp}=\dot{F}_{jm}F^{-1}_{mp}$ and increment of Jacobian given as $J^{\cdot} = \delta_{rs}L_{rs}J$, Eq. (13) can be written as

$$\dot{\sigma}_{ij}=-\delta_{rs}L_{rs}\sigma_{ij}+\hat{\sigma}_{ij}+\sigma_{jm}L_{im}+\sigma_{im}L_{jm} \quad (14)$$

From which the well-known Truesdell stress increment is obtained

$$\hat{\sigma}_{ij}=\dot{\sigma}_{ij}+\delta_{rs}L_{rs}\sigma_{ij}-\sigma_{im}L_{jm}-\sigma_{jm}L_{im} \quad (15)$$

The Truesdell stress increment can be further simplified analogous to Eq. (7) as follows:

$$\hat{\sigma}_{ij}=\frac{1}{V}\int_{\partial V}d\hat{f}^{f}_{i}r_{j}=\gamma_{f}\int_{\partial V}\hat{\sigma}^{f}(\theta,\phi)n_{i}n_{j}\xi(\theta,\phi)\sin\theta d\theta d\phi \quad (16)$$

where the fiber stress increment, $\hat{\sigma^{f}}$, can be related to the fiber strain increment by the following one-dimensional nonlinear constitutive equation considering a slender fiber element:

$$\hat{\sigma}^{f}=C^{f}(e^{f})^{\alpha}\dot{e}^{f} \text{ in tension; and } \hat{\sigma}^{f}=0 \text{ in compression} \quad (17)$$

where C^{f} = constant; and exponent $\alpha \geq 0$. Further, the fiber strain increment, $e^{\cdot f}$, can be expressed in terms of the overall RVE strain increment, $\varepsilon^{\cdot}_{kl}$, using the following kinematic assumption:

$$\dot{e}^{f}=n_{k}n_{l}\dot{\varepsilon}_{kl} \quad (18)$$

Thus, the tangential stress-strain relationship for the RVE can be written as follows:

$$\hat{\sigma}_{ij}=C_{ijkl}\dot{\varepsilon}_{kl} \quad (19)$$

where $C_{ijkl} = \gamma_{f}\int_{\partial V}C^{f}[e^{f}(\theta,\phi)]^{\alpha}n_{i}n_{j}n_{k}n_{l}\xi(\theta,\phi)\sin\theta d\theta d\phi$; and the probability density of the fiber distribution, $\xi(\theta, \phi)$, is discussed in the appendix. The derived relationship has similarities with those obtained using the virtual internal bond and granular micro-mechanics methods (Chang and Misra 1990; Gao and Klein 1998; Misra and Singh (2013); Misra and Yang 2010). The approach presented here can also be applied to obtain higher-order stiffness tensors of relevance to second-gradient and higher-gradient theories (dell'Isola et al. 2009b; Yang et al. 2011; Yang and Misra 2012).

Volumetric Water Content—For the case 1 loading increment, because the fluid pressure increment is held at zero, the incremental change in volumetric water content is the same as the incremental change in volume of pore space, thus

$$\dot{\varsigma}=\varphi\dot{\varepsilon}_{ii}^{\varphi} \quad (20)$$

where $\dot{\varsigma}$ = incremental change in volumetric water content; ϕ = pore volume fraction (porosity) referred to the deformed configuration at the beginning of the strain increment; and $\dot{\varepsilon}_{ii}^{\varphi}$ = increment of average pore space strain. The fiber volume fraction, γ_f, and porosity, ϕ, satisfy the relationship $\gamma_f + \phi = 1$. Further, the incremental average pore space strain can be expressed in terms of the average incremental Green-Lagrange strain of the RVE as follows:

$$\dot{\varepsilon}_{ij}^{\varphi}=H_{ijkl}^{\varphi}\dot{\varepsilon}_{kl} \quad (21)$$

where H_{ijkl}^{φ} = strain concentration tensor for the pore space. The average incremental fiber strain $\dot{\varepsilon}_{kl}^{f}$ can also be expressed in terms of the average incremental Green-Lagrange strain of the RVE as follows:

$$\dot{\varepsilon}_{ij}^{f}=H_{ijkl}^{f}\dot{\varepsilon}_{kl} \quad (22)$$

Following Hill's volume averaging principle expressed as

$$\dot{\varepsilon}_{ij}=(1-\varphi)\dot{\varepsilon}_{ij}^{f}+\varphi\dot{\varepsilon}_{ij}^{\varphi} \quad (23)$$

the following identity is obtained:

$$\delta_{ik}\delta_{jl}=(1-\varphi)H_{ijkl}^{f}+\varphi H_{ijkl}^{\varphi} \quad (24)$$

Noting that the increment of the pore stress is zero, the volume average incremental stress for the RVE can be written as

$$\hat{\sigma}_{ij}=(1-\varphi)\hat{\sigma}_{ij}^{f} \quad (25)$$

Using the constitutive relationship for the fiber material, written as $\hat{\sigma}_{ij}^{f}=C_{ijkl}^{f}\dot{\varepsilon}_{kl}^{f}$, and combining Eqs. (19), (22), and (25), it is found that

$$(1-\varphi)H_{ijkl}^{f}=(C_{pqij}^{f})^{-1}C_{pqkl} \quad (26)$$

Further, using Eqs. (20), (21), (24), and (26), the incremental change in volumetric water content, $\dot{\varsigma}$, can be expressed in terms of the average incremental Green-Lagrange strain of the RVE as

$$\dot{\varsigma}=(\delta_{ik}\delta_{jl}-(C^{f}_{ijkl})^{-1}C_{ijmn})\delta_{ij}\dot{\varepsilon}_{kl} \quad (27)$$

Case 2: ($\dot{\varepsilon}$ =0, $\dot{p}$ ≠ 0)

Because the incremental strain is held to zero during case 2 loading, the increment of Cauchy stress is considered, given as

$$\dot{\sigma}_{ij}=-B_{ij}\dot{p} \quad (28)$$

where $\dot{p}$ = increment of the pore fluid pressure; and B_{ij} = poromechanical parameter. Further, the incremental change in volumetric water content is given as

$$\dot{\varsigma}=\left(\dot{\varepsilon}^{\varphi}_{ii}+\frac{\dot{p}}{K_f}\right)\varphi \quad (29)$$

where the first term arises from the volume change of the pore spaces; and the second term is contributed by the fluid compressibility. In addition, the volume average incremental stress for the RVE can be written as

$$\dot{\sigma}_{ij}=(1-\varphi)\dot{\sigma}^{f}_{ij}+\varphi\dot{\sigma}^{\varphi}_{ij}=(1-\varphi)\dot{\sigma}^{f}_{ij}-\varphi\dot{p}\delta_{ij} \quad (30)$$

Because the fiber material is expected to be considerably (order of magnitude) stiffer than the RVE such that it suffers small deformations, it is assumed that $\dot{\sigma}^{f}_{ij}=C^{f}_{ijkl}\dot{\varepsilon}^{f}_{kl}$, which leads to the following relationship in light of Eq. (28):

$$(1-\varphi)\dot{\varepsilon}^{f}_{kl}=(C^{f}_{ijkl})^{-1}(\varphi\delta_{ij}-B_{ij})\dot{p} \quad (31)$$

Now, using Eq. (23) for this case gets

$$\varphi\dot{\varepsilon}^{\varphi}_{ii}=-(C^{f}_{ijkl})^{-1}(\varphi\delta_{ij}-B_{ij})\dot{p} \quad (32)$$

Thus, from Eq. (29), the incremental change in volumetric water content is obtained as

$$\dot{\varsigma}=\left[-(C^{f}_{pqij})^{-1}(\varphi\delta_{pq}-B_{pq})\delta_{ij}+\frac{\varphi}{K_f}\right]\dot{p} \quad (33)$$

Superposition of Case 1 and Case 2

Case 1 and 2 results, given in Eqs. (19), (27), (28), and (33), are now superposed to obtain the incremental stress-strain relationship for the general case of applied loading, ($\dot{\varepsilon}$, $\dot{p}$), as follows:

$$\dot{\sigma}_{ij} = -\delta_{rs}L_{rs}\overline{\sigma}_{ij} + C_{ijkl}\dot{\varepsilon}_{kl} + \overline{\sigma}_{jm}L_{im} + \overline{\sigma}_{im}L_{jm} - B_{ij}\dot{p} \quad (34)$$

$$\dot{\varsigma} = [\delta_{ik}\delta_{jl} - (C^{f}_{ijkl})^{-1}C_{ijmn}]\delta_{ij}\dot{\varepsilon}_{kl} + \Gamma\dot{p} \quad (35)$$

where $\bar{\sigma}_{ij}$ = effective stress obtained from accretion of Eq. (14), and

$$\Gamma = (C^{f}_{pqij})^{-1}(B_{pq} - \varphi\delta_{pq})\delta_{ij} + \frac{\varphi}{K_f} \quad (36)$$

It now remains to define B_{ij}, to which end the following second-order virtual work expression is considered:

$$\dot{\sigma}^{2}_{ij}\delta\dot{\varepsilon}^{1}_{ij} = \left\langle \dot{\sigma}^{2}_{ij}\delta\dot{\varepsilon}^{1}_{ij} \right\rangle_{V} = (1-\varphi)\left\langle \dot{\sigma}^{f2}_{ij}\delta\dot{\varepsilon}^{f1}_{ij} \right\rangle_{V_f} + \varphi\left\langle \dot{\sigma}^{\varphi 2}_{ij}\delta\dot{\varepsilon}^{\varphi 1}_{ij} \right\rangle_{V_\varphi} \quad (37)$$

where $\langle . \rangle$ = volume-averaged quantities; and superscripts represent cases 1 and 2. In light of Eqs. (28), (30), and (31), Eq. (37) becomes

$$-B_{ij}\dot{p}\delta\dot{\varepsilon}^{1}_{ij} = (1-\varphi)\dot{\sigma}^{f1}_{ij}\delta\dot{\varepsilon}^{f2}_{ij} - \varphi\dot{p}\delta_{ij}\delta\dot{\varepsilon}^{\varphi 1}_{ij} \quad (38)$$

It is straightforward to show that the first term of the right-hand side vanishes, that is $\dot{\sigma}^{f1}_{ij}\delta\dot{\varepsilon}^{f2}_{ij} = 0$ by considering the second-order virtual work $\left\langle \dot{\sigma}^{1}_{ij}\delta\dot{\varepsilon}^{2}_{ij} \right\rangle_{V}$ Now, using Eq. (21), the second-order virtual work expression in Eq. (38) is simplified as follows:

$$B_{ij}\dot{p}\delta\dot{\varepsilon}^{1}_{ij} = \varphi\dot{p}\delta_{ij}H^{\varphi}_{ijkl}\delta\dot{\varepsilon}^{1}_{kl} \quad (39)$$

Because Eq. (39) must hold for all virtual strain increments, $\delta\dot{\varepsilon}^{1}_{kl}$, the following expression is obtained for B_{ij} using Eqs. (24) and (26):

$$B_{ij} = [\delta_{mi}\delta_{nj} - (C^{f}_{pqmn})^{-1}C_{pqij}]\delta_{mn} \quad (40)$$

Thus, Eqs. (34)–(36) can be written as follows:

$$\dot{\sigma}_{ij} = -\delta_{rs}L_{rs}\overline{\sigma}_{ij} + C_{ijkl}\dot{\varepsilon}_{kl} + \overline{\sigma}_{jm}L_{im} + \overline{\sigma}_{im}L_{jm} - B_{ij}\dot{p} \quad (41)$$

$$\dot{\varsigma}=B_{ij}\dot{\epsilon}_{ij}+\Gamma\dot{p} \quad (42)$$

$$\Gamma=(C^f_{ijkl})^{-1}\{[\delta_{mi}\delta_{nj}-(C^f_{pqmn})^{-1}C_{pqij}]\delta_{mn}-\varphi\delta_{ij}\}\delta_{kl}+\frac{\varphi}{K_f} \quad (43)$$

Comparison of Drained and Undrained Compression

For the examples discussed hereafter, the RVE is subjected to unconfined uniaxial loading in two separate phases: the free swell phase followed by either drained or undrained loading under uniaxial stress conditions.

Loading Conditions

Free Swelling—In the free swell phase, the RVE undergoes prestrain because of swelling caused by water migration in response to the chemical potential difference between the material and the environment under an overall stress-free condition. The phenomena results in an osmotic pore pressure in the RVE fluid phase. At equilibrium, in which chemical potential difference vanishes, osmotic pore pressure, p^c, can be obtained using Donnan's method as follows: (Overbeek 1956)

$$p=p^c=RT[(0.25C_F^2+C_o^2)^{1/2}-C_o] \quad (44)$$

where C_F = fixed charge density of the material; C_o = molarity of the salt solution in which the RVE is immersed; R = universal gas constant; and T = temperature. The prestrain and pore pressure increments can now be obtained from Eqs. (41) and (42) by setting the stress increment to zero, such that

$$\dot{p}=\frac{1}{\Gamma}(\dot{\varsigma}-B_{kl}\dot{\varepsilon}_{kl}) \quad (45)$$

$$\dot{\varepsilon}_{kl}=\left(C_{ijkl}+\frac{1}{\Gamma}B_{ij}B_{kl}\right)^{-1}\left(\delta_{rs}L_{rs}\overline{\sigma}_{ij}-\overline{\sigma}_{jm}L_{im}-\overline{\sigma}_{im}L_{jm}+B_{ij}\frac{\dot{\varsigma}}{\Gamma}\right) \quad (46)$$

where the incremental volumetric water content $\dot{\varsigma}$ is specified using suitable step size. To estimate the step size, the prestrain is approximated using Eq. (41) and the total volumetric water content change under small-strain linear assumption. The step-size $\dot{\varsigma}$ is then taken as a fraction (typically 1=100th) of the approximated total volumetric water content change. The incremental strains are accumulated to obtain the prestrain corresponding to the equilibrium osmotic pore pressure.

Undrained Loading—During undrained loading, there is no ingress or egress of water, and the incremental volumetric water content, $\dot{\varsigma}$, is set to zero. Thus, from Eqs. (41) and (42)

$$\dot{p} = -\frac{1}{\Gamma} B_{kl} \dot{\varepsilon}_{kl} \quad (47)$$

$$\dot{\varepsilon}_{kl} = \left(C_{ijkl} + \frac{1}{\Gamma} B_{ij} B_{kl} \right)^{-1} (\dot{\sigma}_{ij} + \delta_{rs} L_{rs} \overline{\sigma}_{ij} - \overline{\sigma}_{jm} L_{im} - \overline{\sigma}_{im} L_{jm}) \quad (48)$$

Further, the volume fractions of the constituents change during loading. From Eq. (29), the incremental change of porosity is given as

$$\dot{\varphi} = -\varphi \left(\frac{\dot{p}}{K_f} + \frac{\dot{J}}{J} \right) \quad (49)$$

The volume fraction of the fiber is calculated from the identity, $\gamma_f + \phi = 1$, and the increment of fixed charge density is given as

$$\dot{C}_F = -C_F \dot{\varepsilon}_{ii}^{\varphi} \quad (50)$$

Drained Loading—During drained loading, ingress or egress of water is permitted such that when equilibrium is reached for an applied load, the pore pressure is the same as the osmotic pore pressure. In this case, Eqs. (41) and (42) apply directly. Further, the incremental change of porosity is obtained from Eq. (29), and the increment of fixed charge density is given by Eq. (50).

Results and Discussions

The parameters used for the calculations described subsequently are taken to be as follows: one-dimensional constitutive law for fiber $-a = 0.5$, $C^f = 1{,}200$ MPa, fiber volume fraction in the reference state $\gamma_f = 0.55$, porosity in the reference state, $\phi = 0.45$, fixed charge density in the reference state $C_F = 330$ meq/m^3, external salt concentration $C_o = 15$ meq/m^3, fiber material properties—Young's modulus = 200 MPa, Poisson's ratio = 0.2, bulk modulus of water $K_f = 2{,}200$ MPa, and the probability density function of initially isotropic fiber distribution given by Eq. (52). These model parameters are chosen to enable a qualitative comparison with the behavior of articular cartilage, which is an example of a chemically active water saturated fibrous material (Oloyede et al. 1992).

Fiber Stress and Induced Anisotropy

In the free swelling phase, during which water is free to drain, an isotropic prestrain of 1.27% develops. Thus, at the end of the free swelling phase, all the fibers in the network are under equal tension, as shown in Fig. 3, which gives the directional fiber stress distribution at 0, 0.8, 2.5, and 10% axial strain, respectively. Under free swelling conditions, the fiber network behaves as an isotropic material. Because the RVE is subjected to compressive uniaxial stress loading, fibers oriented closer to the loading direction experience unloading, whereas those closer to the lateral direction experience further tensile loading, as shown by

the directional fiber stress distribution in Fig. 3. Consequently, the fiber network behaves as a transverse isotropic material, although the degree and the nature of this induced anisotropy depend on the drainage condition. The predicted overall stress-strain behavior and the evolution of material parameters for the two drainage conditions are shown in Figs. 4 and 5. In Figs. 3–6, the axial strain is expressed with respect to the free swollen configuration, such that 0% axial strain corresponds to the end of the free swelling phase.

Stress-Strain and Pore Pressure-Water Content

Fig. 4(a) gives the plot of the axial stress, σ_{11}, with axial strain, ε_{11}, and lateral strain, ε_{22}, during the uniaxial loading. Fig. 4(a) shows that in the initial stages of loading, for axial strain magnitude, ε_{11}, below the tensile prestrain, the overall stress-strain behavior of the drained and undrained cases are close. However, the drained and undrained behaviors deviate considerably once the fibers oriented closer to the axial direction completely unload. Further, from Fig. 4(b), it is observed that for the drained case, the axial effective stress attributable to the fiber network decreases rapidly from its initial tensile state. In this case, the applied axial stress is increasingly supported by the pore pressure, which for the drained case is contributed to exclusively by the osmotic pore pressure, as seen from Fig. 4(d). The rise in osmotic pore pressure for the drained condition is not unexpected because there is a considerable increase in fixed charge density because of the volume compression and change in porosity, as shown in Figs. 4(c and d), respectively.

In contrast, for the undrained case, the axial effective stress first decreases and then begins to increase, as seen from Fig. 4(b). In this case, the large tensile loading that the lateral fibers experience makes increasing contribution to the axial component of the effective stress. This aspect is further expounded on in the subsection “Evolution of Stiffness and Poromechanical Parameters.” The contribution of the pore pressure in supporting the applied stress is significantly higher for the undrained case, as seen in Figs. 4(e and f). In this case, the osmotic pore pressure contribution is insignificant because there is negligible change in fixed charge density and the porosity [Figs. 4(c and d), respectively].

The uniaxial stress-strain behavior for the undrained and drained cases closely resemble the bounds of experimental data presented by Oloyede et al. (1992) for extremely low (close to drained conditions) and extremely high (close to undrained conditions) loading rates, respectively. The absence of an initially stiff region in the data presented by Oloyede et al. (1992) is expectant because of the relatively high bath salt concentration of 0.15 M in their experiments. In this example's calculations, given in Fig. 3, a lower bath salt concentration of 0.015 M is used to demonstrate the effect of higher prestrain. Similar results to Oloyede et al. (1992) are obtained for higher bath salt concentration. Further, the apparent yielding in the stress-strain curve for the drained case predicted by the model has also been observed in experiments on free-swollen articular cartilage (Chahine et al. 2004). According to this model prediction, the postyield behavior is primarily governed by the osmotic pressure. Similar postyield behavior has also been observed in experiments under drained conditions (Chahine et al. 2004). Moreover, the stiffness in the postyield regime is found to have a small increase (DiSilvestro et al. 2001) that agrees with the prediction shown in Fig. 4(a). The apparent yielding is absent at a higher rate of loading (Li et al. 2003), which is similar

to the undrained behavior predicted by this model. Further, the load sharing between the fiber network and the pore fluid predicted for undrained compression agrees with the well-accepted hypothesis that the pore-pressure largely supports the applied load in the early part of the time response of the articular cartilage (Li et al. 2003; Li and Herzog 2004; Soltz and Gerard 1998).

Evolution of Stiffness and Poromechanical Parameters

The behavior in the two drainage conditions is further described by considering the evolution of the material parameters during loading. Figs. 5(a–c) give the plots of normalized fiber network stiffnesses, C_{1111} and C_{2222} and Poisson's ratio, ν_{12}, respectively. The pore pressure in the RVE is governed by the parameter, Γ, whereas its contribution to the overall stress is modulated by the parameter B_{ij}. Figs. 5(d–f) give the plot of the evolution of normalized Γ, B_{11}, and B_{22}, respectively.

Fig. 5(a) shows that the fiber network stiffness C_{1111} decays for both drained and undrained conditions to an asymptotic value. For the drained case, the stiffness C_{1111} is generally smaller than that of the undrained case, except in the initial part of the loading. In comparison, Fig. 5(b) shows that fiber network stiffness C_{2222} increases monotonically for the undrained case. For the drained case, C_{2222} first increases and then decreases in a comparatively narrow range. The differences in fiber network stiffness can be attributed to the fiber stress distribution in the two cases shown in Fig. 3. In the early stages of loading, the fibers oriented closer to the loading direction resist a significant part of the applied axial stress for the two cases. As the axial strain increases, the fibers oriented close to the loading direction completely unload, whereas those oriented closer to the lateral direction experience further tensile loading. However, the fiber stresses for the undrained case remain generally larger than that for the drained case, as seen from Fig. 3. The increase in the tensile loading of the fibers oriented laterally is predicted by Eq. (41), which says that the pore pressure and the fiber stress must equilibrate one another in the lateral direction in the unconfined case. As a result, the fibers oriented laterally become stiffer. Because the pore pressure increase is substantially greater in the case of undrained loading, the fiber network stiffness is also larger. For the drained loading case, the stiffening effect in the lateral direction is relatively smaller.

Fig. 5(c) gives the apparent Poisson's ratio, ν_{12}, for the two drainage conditions. This apparent Poisson's ratio is computed as the ratio of the lateral to the axial strain with reference to the free swollen state as typically done in experiments. For the un-drained case, it is observed that this Poisson's ratio rapidly asymptotes to 0.5. For the drained case, the apparent Poisson's ratio decreases from a value of approximately 0.3 as fluid is squeezed out during compression. Similar strain dependence of Poisson's ratio has been reported from drained uniaxial compression of articular cartilage (Chahine et al. 2004). The decrease in Poisson's ratio is attributed to the rapid loss in overall stiffness in the direction of loading relative to the lateral direction. The absence of the mechanical pressure in pore fluid as seen from Fig. 4(f) also contributes to the loss of stiffness in the drained case.

Figs. 5(d and e) give a plot of the evolution of parameters B_{11} and B_{22}. Recall from Eq. (40) that B_{ij} represents the relative stiffness of the fiber network with respect to the fiber material. When the fiber network stiffness is small relative to the fiber material, B_{ij} tends to identity. Therefore, it is not surprising that in the drained case, both B_{11} and B_{22} tend to increase as the fiber network stiffness generally decreases with loading. A similar damage-induced increase in the values of B_{11} and B_{22} has been predicted for poroelastic solids (Lydzba and Shao 2000). Moreover, B_{11} and B_{22} reflect the effects of loading-induced anisotropy similar to that predicted for linear poroelastic material undergoing damage (Lydzba and Shao 2000). In contrast, for the undrained case, B_{11} increases as the fiber network softens in the axial direction; however, B_{22} decreases in response to the stiffening of the fiber network in the lateral direction discussed previously. Similarly, parameter Γ increases for the drained case as the fiber network becomes soft and more compressible with loading. However, for the undrained case, parameter Γ first increases, but then decreases as the overall compressibility of the fiber network also changes in a similar manner. In this case, the fiber network stiffness in the axial direction decreases, whereas that in the lateral direction increases. The overall effect of these competing phenomena is represented in parameter Γ. In traditional models for these types of materials, it is typical to assume $B_{ij} = \delta_{ij}$ and $\Gamma = 0$. Although these may be reasonable approximations at large strains, it is important to have a more accurate value at smaller strains to obtain correct effects of the pore pressure.

Effect of Fiber Nonlinearity

The fiber has been assumed to have a nonlinear behavior under tension arising from geometrical effects such as fiber crimping, braiding, or folding. Here the effect of fiber nonlinearity is explored by investigating the drained behavior for exponent $a = 0$, 0.1, and 0.5. So that the comparison is on a similar footing, it is assumed that the fiber behavior is the same at a fiber strain of 30%, as shown in Fig. 6(a), such that the parameter $C^f = 666.7$, 827.2, and 1,800 MPa, respectively, for the three cases. From Fig. 6(b), it can be seen that the fiber nonlinearity significantly affects the stiffness in the drained condition. Because of different nonlinearity, the prestrain in the three cases is different. Therefore, the softening of the fiber network commences at different applied axial strain, as seen from Fig. 6(c). The behavior of the RVE for linear fiber is stiffer than that of the nonlinear fiber, although the prestrain for linear fiber is smaller. Such a result is expected because the linear fiber is generally stiffer at small strains compared to nonlinear fiber. In addition, Fig. 6(b) shows that the behavior at larger strains is primarily governed by the osmotic pressure and has insignificant influence of the fiber-nonlinearity. Clearly, the fiber stiffness and nonlinearity has impact on the prediction of swelling and stress-strain behavior. Such prediction can be of significance in assessing disease states of soft tissues (Bank et al. 2000).

Fig. 6(d) also shows that the lateral stiffness varies little for RVE with nonlinear fiber, but decreases significantly for linear fibers. The lateral stiffness evolution is a complex function of the osmotic pressure and the fiber unloading. Further, from Figs. 6(e and f),it is noted that the RVE with nonlinear fibers are relatively softer than the fiber material; therefore, parameter B_{11} is closer to 1, and parameter Γ is larger because the fiber network is more compressible at the prestrained condition. As the loading progresses, the fibers unload, and RVE stiffness becomes smaller for all cases. Thus, parameter B_{11}, for all three cases,

approaches unity. Similarly, the parameter Γ also tends to a common compressibility with loading. The comparison of behavior for different fiber nonlinearity shows that the overall material nonlinearity can be attributed to two phenomena: (1) fiber buckling as the fibers unload; and (2) intrinsic fiber nonlinearity. The former is a purely microstructural phenomenon resulting from the high aspect ratio of a fiber, whereas the latter is attributable to the nonlinearity in the fiber.

Summary and Conclusions

The authors have presented a derivation of poromechanical theory of fluid-saturated chemically active fibrous media. In the derived theory, the tangent stiffness of the dry fiber network is obtained using the framework of granular micromechanics. The poromechanics constitutive relationships are then obtained using Hill's volume averaging principles for strain-free and pore-pressure free conditions. To account for fiber nonlinearity and large deformations, the equations are formulated in an incremental form. The resultant model gives expressions for (1) the fiber network tangent stiffness, C_{ijkl}, in terms of the fiber mechanical properties and fiber directional distribution; (2) the poromechanical parameter, B_{ij}, in terms of the relative stiffness of the fiber network with respect to the fiber material; and (3) the poromechanical parameter, Γ, in terms of the relative compressibility of the fiber network and the fluid phase. The osmotic pressure that develops because of the chemical activity of the fiber network is modeled using Donnan's method. Thus, the derived theory provides a method determining the contributions of the mechanical aspects and chemical aspects to the load-bearing abilities of these materials.

The applicability of the model is demonstrated by comparison with the observed drained and undrained behaviors of articular cartilage under uniaxial compressive stress. The model predictions are found to show similar trends of stress-strain behavior, as experimentally observed. The model is able to predict the apparent yield observed under drained conditions, and its absence in the undrained condition. The model also exhibits the postyield stiffening behavior and the reduction in Poisson's ratio in the drained conditions. The authors also demonstrated the effect of microscale phenomena such as fiber buckling on the macroscale stiffness tensor and poromechanics parameters. In addition, the authors demonstrated the effect of fiber nonlinearity on the overall behavior. Traditionally, the constitutive laws used to describe these materials have assumed poromechanical parameter B to be unity and Γ to be zero. In the theory presented here, the poromechanical parameters can be calculated under a given set of loading conditions.

In this paper, only results for monotonic static loading under drained or undrained conditions have been presented. The model can be utilized to obtain the rate-dependent behavior of poromechanical materials. For example, the derived model provides a method for determining the load sharing between the fiber network and the pore fluid, which is of interest in transient behavior of these materials (Li and Herzog 2004). It is further noted that the analysis presented here is focused on a system in which the solid matrix is composed of a fibrous network. However, the presented methodology can be extended to other materials such as clays, polymers, and hydrogels. Furthermore, it is noted that for the porous materials of the type considered here, the behavior may be affected by other microscale phenomena,

such as capillarity, and by occurrence of thin boundary layers that are best modeled using higher-gradient approaches (dell'Isola et al. 2009a; Madeo et al. 2008; Sciarra et al. 2008). The present methodology can be potentially applied to obtain the relevant constitutive parameters for these higher-gradient poromechanical theories.

Acknowledgments

This research is supported in part by USPHS Research Grant NIH/NIDCR DE014392 (PS), NIH/NIDCR DE022054 (PS), and NSF grant CMMI-1068528 (AM).

Appendix. Fiber Orientation Density Function

The fiber orientation density function expressed in spherical coordinates, $\xi_1(\theta, \phi)$, is written in a discrete form as follows:

$$\xi(n_i)=\frac{1}{M}\sum_{j=1}^{M}\delta(n_i - n_i^j) \quad (51)$$

where M = total number of fibers; $\delta(\boldsymbol{n} - \boldsymbol{n}^j) = \delta(\theta - \theta^j)\,\delta(\phi - \phi^j)/\sin\theta$, δ = Dirac delta; and the superscript j refers to the observed fiber directions. The observed discrete directional density of the type given by Eq. (51) can be estimated as a smooth orientation distribution function by fitting with parametric forms discussed by (Kanatani 1984). Other forms of smooth orientation distribution functions, particularly exponential forms that appear as extensions of von Mises or Fisher distributions, may be used, especially when they are needed to represent highly directional data (Cortes et al. (2010); Federico and Herzog 2008a, b). For practical calculations, transversely isotropic fiber orientation can be expressed as (Chang and Misra 1990)

$$\xi(\theta,\varphi)=\frac{1}{4}\frac{1+(1/4)a_{20}[3\cos(2\theta)+1]}{\pi} \quad (52)$$

where a_{20} = anisotropy factor, such that the isotropic fiber orientation can be expressed as ($a_{20} = 0$)

$$\xi(\theta,\varphi)=\frac{1}{4\pi} \quad (53)$$

References

Ateshian GA, Rajan V, Chahine NO, Canal CE, Hung CT. Modeling the matrix of articular cartilage using a continuous fiber angular distribution predicts many observed phenomena. J Biomech Eng. 2009; 131(6):1–10.

Bank RA, Soudry M, Maroudas A, Mizrahi J, TeKoppele JM. The increased swelling and instantaneous deformation of osteoarthritic cartilage is highly correlated with collagen degradation. Arthritis Rheumatism. 2000; 43(10):2202–2210. [PubMed: 11037879]

Bennethum LS, Cushman JH. Multiscale, hybrid mixture theory for swelling systems—II: Constitutive theory. Int J Eng Sci. 1996; 34(2):147–169.

Bennethum LS, Murad MA, Cushman JH. Modified Darcy's law, Terzaghi's effective stress principle and Fick's law for swelling clay soils. Comput Geotech. 1997; 20(3):245–266.

Biot MA. General theory of three-dimensional consolidation. J Appl Phys. 1941; 12(2):155–164.

Biot MA. Theory of finite deformations of porous solids. Indiana Univ Math J. 1972; 21(7):597–620.

Cariou, S.; Dormieux, L.; Skoczylas, F. ECCOMAS Multidisciplinary Jubilee Symp. Springer; Dordrecht: 2009. Swelling of a benton-ite plug: A micromechanical approach; p. 63-77.

Chahine NO, Wang CCB, Hung CT, Ateshian GA. Anisotropic Strain Dependent Material Properties of Bovine Articular Cartilage in the Transitional Range from tension to compression. Journal of Biomechanics. 2004; 37(8):1251–1261. [PubMed: 15212931]

Chang CS, Misra A. Theoretical and experimental study of regular packings of granules. J Eng Mech. 1989; 115(4):704–720.

Chang CS, Misra A. Packing structure and mechanical properties of granulates. J Eng Mech. 1990; 116(5):1077–1093.

Cortes DH, Lake SP, Kadlowec JA, Soslowsky LJ, Elliott DM. Characterizing the mechanical contribution of fiber angular distribution in connective tissue: Comparison of two modeling approaches. Biomech Model Mechanobiol. 2010; 9(5):651–658. [PubMed: 20148345]

de Buhan P, Chateau X, Dormieux L. The constitutive equations of finite strain poroelasticity in the light of a micro-macro approach. Eur J Mech A Solids. 1998; 17(6):909–921.

dell'Isola F, Madeo A, Seppecher P. Boundary conditions at fluid-permeable interfaces in porous media: A variational approach. Int J Solids Struct. 2009a; 46(17):3150–3164.

dell'Isola F, Sciarra G, Vidoli S. Generalized Hooke's law for isotropic second gradient materials. Proc R Soc A Math Phys Eng Sci. 2009b; 34(2107):2177–2196.

DiSilvestro MR, Zhu QL, Suh JKF. Biphasic poroviscoelastic simulation of the unconfined compression of articular cartilage: II—Effect of variable strain rates. J Biomech Eng. 2001; 123(2):198–200. [PubMed: 11340882]

Dormieux L, Lemarchand E, Coussy O. Macroscopic and micromechanical approaches to the modelling of the osmotic swelling in clays. Transp Porous Media. 2003; 50(1–2):75–91.

Dormieux L, Molinari A, Kondo D. Micromechanical approach to the behavior of poroelastic materials. J Mech Phys Solids. 2002; 50(10):2203–2231.

Federico S, Herzog W. On the anisotropy and inhomogeneity of permeability in articular cartilage. Biomech Model Mechanobiol. 2008a; 7(5):367–378. [PubMed: 17619089]

Federico S, Herzog W. Towards an analytical model of soft biological tissues. J Biomech. 2008b; 41(16):3309–3313. [PubMed: 18922533]

Gao HJ, Klein P. Numerical simulation of crack growth in an isotropic solid with randomized internal cohesive bonds. J Mech Phys Solids. 1998; 46(2):187–218.

Kanatani KI. Distribution of directional-data and fabric tensors. Int J Eng Sci. 1984; 22(2):149–164.

Lai WM, Hou JS, Mow VC. A triphasic theory for the swelling and deformation behaviors of articular cartilage. J Biomech Eng. 1991; 113(3):245–258. [PubMed: 1921350]

Li LP, Buschmann MD, Shirazi-Adl A. Strain-rate dependent stiffness of articular cartilage in unconfined compression. Trans Am Soc Mech Eng J Biomech Eng. 2003; 125(2):161–168.

Li LP, Herzog W. Strain-rate dependence of cartilage stiffness in unconfined compression: The role of fibril reinforcement versus tissue volume change in fluid pressurization. J Biomech. 2004; 37(3): 375–382. [PubMed: 14757457]

Loret B, Simoes FMF. Effects of the pH on the mechanical behavior of articular cartilage and corneal stroma. Int J Solids Struct. 2010; 47(17):2201–2214.

Lydzba D, Shao J. Study of poroelasticity material coefficients as response of microstructure. Mech Cohesive Frictional Mater. 2000; 5(2):149–171.

Madeo A, Dell'Isola F, Ianiro N, Sciarra G. A variational deduction of second gradient poroelasticity II: An application to the consolidation problem. J Mech Mater Struct. 2008; 3(4):607–625.

Misra A, Chang CS. Effective elastic moduli of heterogeneous granular solids. Int J Solids Struct. 1993; 30(18):2547–2566.

Misra A, Marangos O, Parthasarathy R, Spencer P. Micro-scale analysis of compositional and mechanical properties of dentin using homotopic measurements. Lect Notes Comput Vision Biomech. 2012; 20(3):245–266.

Misra A, Singh V. Micromechanical model for viscoelastic materials undergoing damage. Continuum Mech Thermodyn. 2013; 25(2–4):343–358.

Misra A, Yang Y. Micromechanical model for cohesive materials based upon pseudo-granular structure. Int J Solids Struct. 2010; 47(21):2970–2981.

Mow VC, Kuei SC, Lai WM, Armstrong CG. Biphasic creep and stress relaxation of articular cartilage in compression: Theory and experiments. J Biomech Eng. 1980; 102(1):73–84. [PubMed: 7382457]

Moyne C, Murad MA. Electro-chemo-mechanical couplings in swelling clays derived from a micro/macro-homogenization procedure. Int J Solids Struct. 2002; 39(25):6159–6190.

Moyne C, Murad M. Macroscopic behavior of swelling porous media derived from micromechanical analysis. Transp Porous Media. 2003; 50(1–2):127–151.

Oloyede A, Flachsmann R, Broom ND. The dramatic influence of loading velocity on the compressive response of articular cartilage. Connect Tissue Res. 1992; 27(4):211–224. [PubMed: 1576822]

Overbeek JT. The Donnan equilibrium. Progress Biophys Biophys Chem. 1956; 6(1):57–84.

Sciarra G, Dell'Isola F, Ianiro N, Madeo A. A variational deduction of second gradient poroelasticity part I: General theory. J Mech Mater Struct. 2008; 3(3):507–526.

Signorini A. Sollecitazioni Iperastatiche. Rend Inst Lombardo. 1932; 2(65):1–7.

Soltz MA, Gerard AA. Experimental verification and theoretical prediction of cartilage interstitial fluid pressurization at an impermeable contact interface in confined compression. J Biomech. 1998; 31(10):927–934. [PubMed: 9840758]

Terzaghi K. Principles of soil mechanics. Eng News Rec. 1925; 95(8)

Truesdell, C.; Toupin, R. The classical field theories. Springer; Berlin: 1960.

Wang X, Hong W. A visco-poroelastic theory for polymeric gels. Proc R Soc A Math Phys Eng Sci. 2012; 468(2148):3824–3841.

Yang Y, Ching WY, Misra A. Higher-order continuum theory applied to fracture simulation of nano-scale intergranular glassy film. J Nanomech Micromech. 2011; 1(2):60–71.

Yang Y, Misra A. Micromechanics based second gradient continuum theory for shear band modeling in cohesive granular materials following damage elasticity. Int J Solids Struct. 2012; 49(18):2500–2514.

Yoon J, Cai S, Suo Z, Hayward RC. Poroelastic swelling kinetics of thin hydrogel layers: Comparison of theory and experiment. Soft Matter. 2010; 6(23):6004–6012.

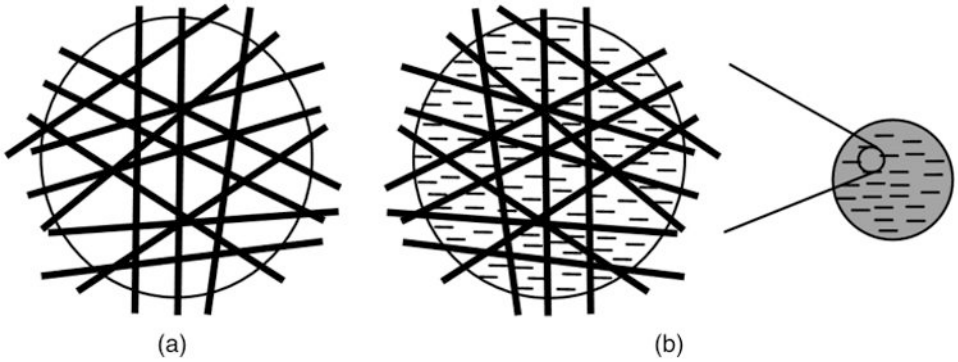

Fig. 1.

(a) Schematic of dry fibrous network at the microscale; (b) schematic of saturated fibrous network at microscale by zooming in to a homogenized representative volume element at the macroscale

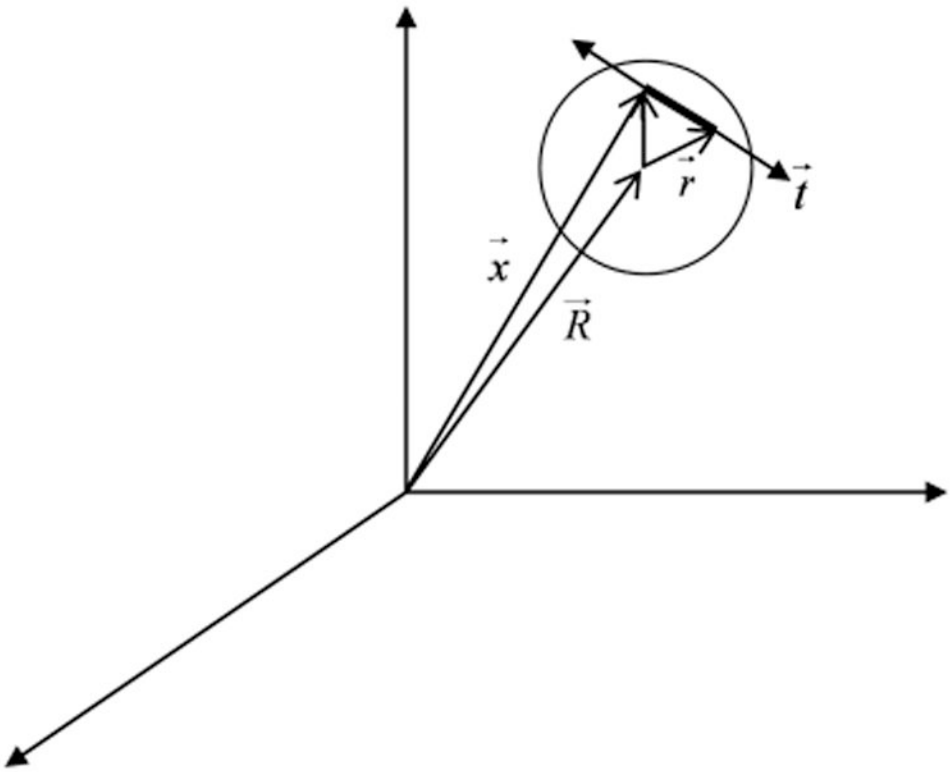

Fig. 2. Fiber traction in an RVE

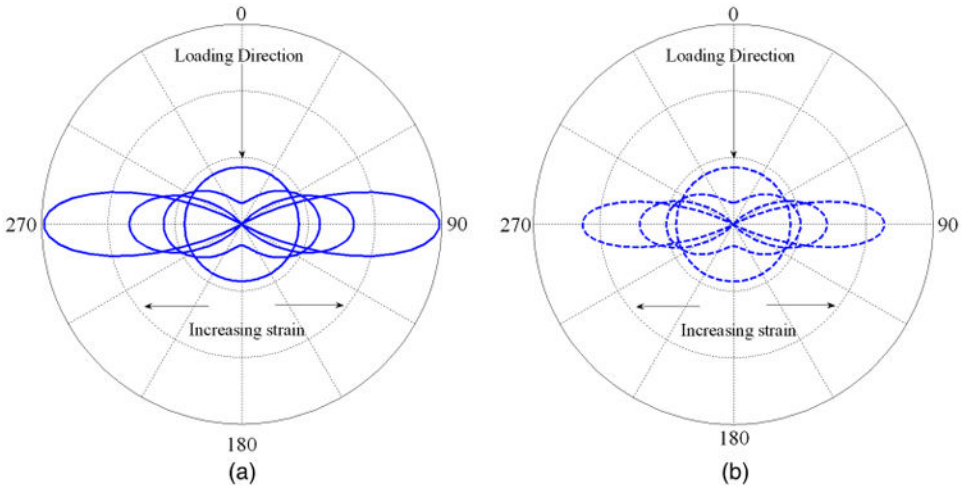

Fig. 3.

Predicted fiber stress distribution with increasing compressive applied strains of 0, 0.8, 2.5, and 10% for (a) undrained; (b) drained conditions (plotted to the same scale)

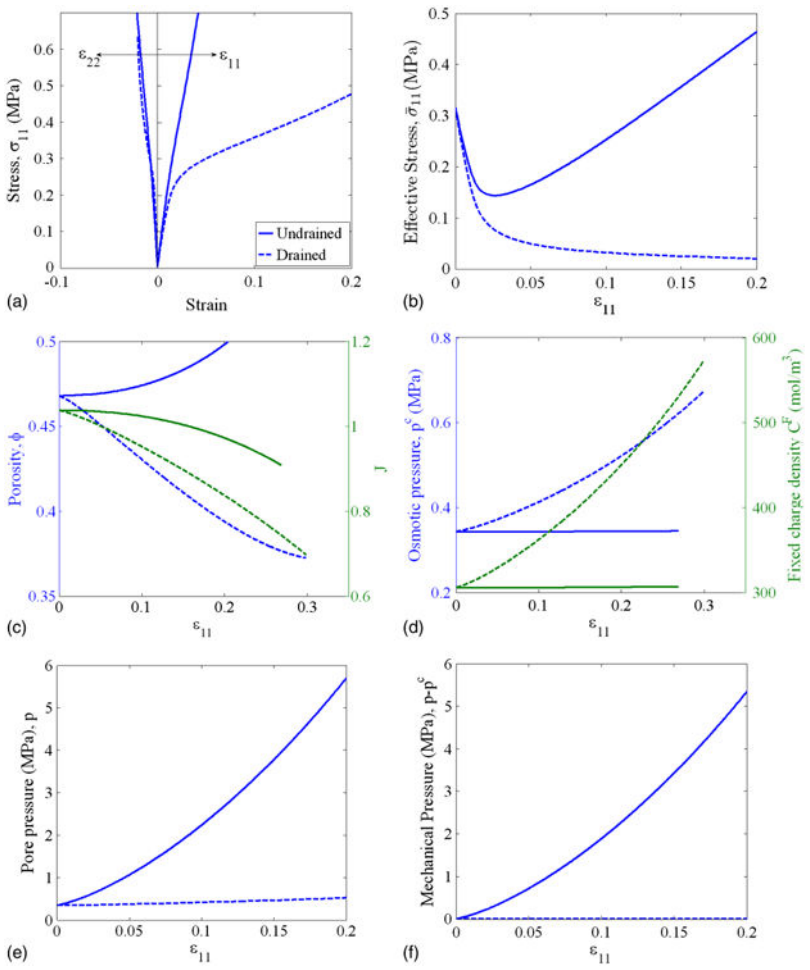

Fig. 4.

Evolution of (a) stress, (b) effective stress, (c) volume change and porosity, (d) osmotic pressure and fixed charge density, (e) pore pressure and (f) mechanical pressure under uniaxial compression for drained and undrained cases of loading

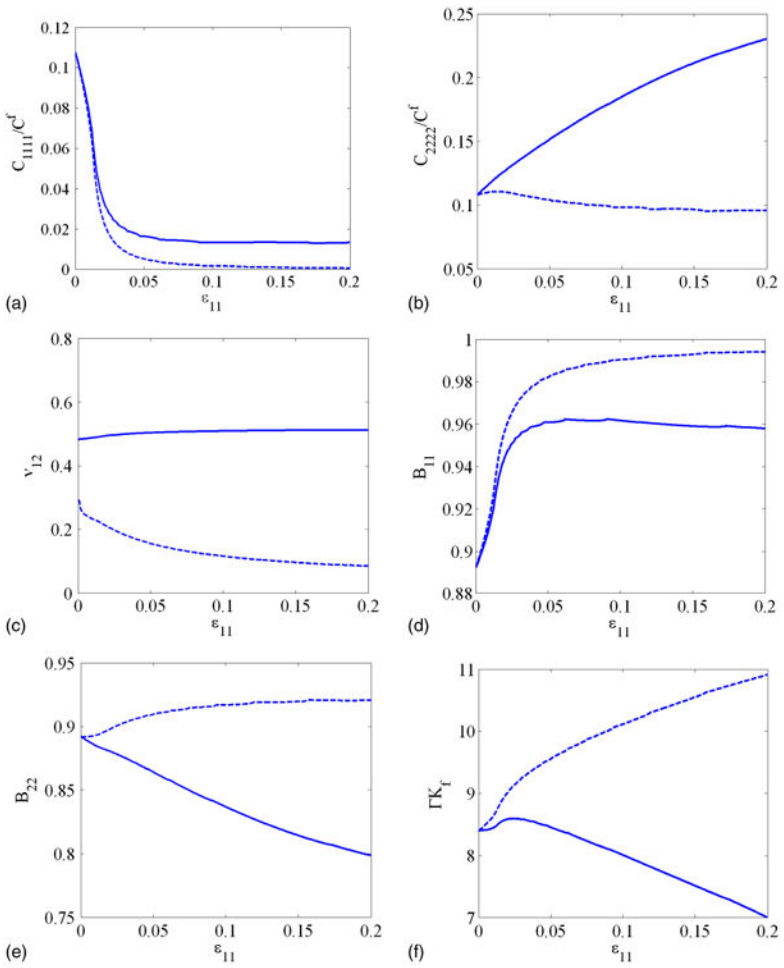

Fig. 5.

Evolution of stiffness and poromechanical parameters under uniaxial compression for drained and undrained cases of loading: (a) fiber network stiffness C_{1111}; (b) fiber network stiffness C_{2222}; (c) apparent Poisson's ratio; (d) poromechanics parameter B_{11}; (e) poromechanics parameter B_{22}; and (f) overall compressibility

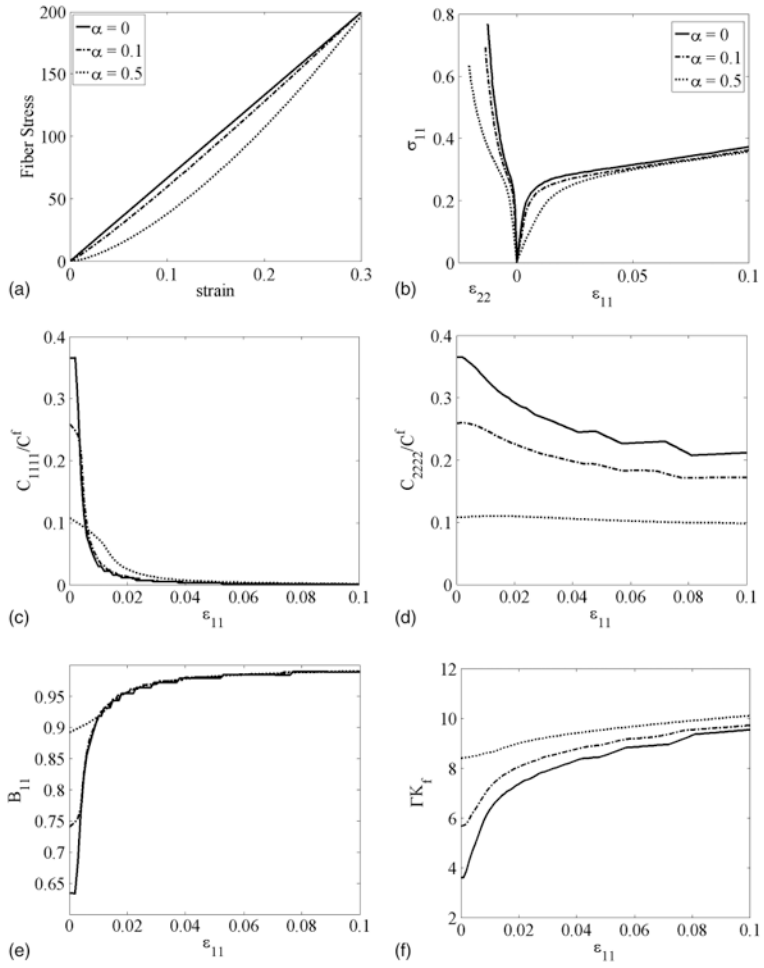

Fig. 6.

Effect of fiber nonlinearity on drained behavior under unconfined compression: (a) fiber behavior; (b) stress-strain behavior; (c) fiber network stiffness C_{1111}; (d) fiber network stiffness C_{2222}; (e) poromechanics parameter B_{11}; and (f) overall compressibility